Acta Materialia 158 (2018) 407–421

Contents lists available at ScienceDirect

Acta Materialia

journal homepage: www.elsevier.com/locate/actamat

Full length article

In-situ TEM observation of $\{10\bar{1}2\}$ twin-dominated deformation of Mg pillars: Twinning mechanism, size effects and rate dependency

Jiwon Jeong [a, b], Markus Alfreider [c], Ruth Konetschnik [c], Daniel Kiener [c], Sang Ho Oh [a, b, *]

[a] Department of Materials Science and Engineering, Pohang University of Science and Technology (POSTECH), Pohang, 37673, Republic of Korea
[b] Department of Energy Science, Sungkyunkwan University, Suwon, 16419, Republic of Korea
[c] Department Materials Physics, Montanuniversität Leoben, Jahnstraße 12, 8700, Leoben, Austria

ARTICLE INFO

Article history:
Received 15 May 2018
Accepted 9 July 2018
Available online 18 July 2018

Keywords:
Magnesium
In-situ TEM
Size effect
Strain rate
Deformation twinning

ABSTRACT

To investigate the mechanism of $\{10\bar{1}2\}$ twinning in magnesium (Mg) single crystal and its influence on mechanical size effects and strain rate dependent deformation behavior, in-situ microcompression of Mg $[2\bar{1}\bar{1}0]$ pillars of various sizes from 0.5 μm to 4 μm was carried out in a scanning electron microscope (SEM) and also in a transmission electron microscope (TEM), covering strain rates from 10^{-4} to 10^{-2} s^{-1}. The in-situ observations directly showed that the pile-up of prismatic <*a*> dislocations acts as local stress concentration for the twin nucleation. Preceding the twin nucleation, the lead dislocation from the dislocation pile-up cross-slips to the basal plane and dissociates into partial dislocations, one of which trails a stacking fault (SF) behind. The twin nucleus of a finite size formed at the junction between prismatic <*a*> dislocations and basal SFs and subsequently propagated rapidly across the pillar. The present in-situ observations reveal that not only the dislocation pile-up but also the dissociation reaction of <*a*> dislocations play critical roles in the nucleation of $\{10\bar{1}2\}$ twins. Furthermore, the $\{10\bar{1}2\}$ twinning exhibits a relatively strong size effect in terms of the twin nucleation stress (size exponent $n = 0.7$). This pronounced size effect may arise from the fact that the precursor to twin nucleation, namely dislocation pile-up and junction formation, depends more strongly on the crystal size than the ordinary dislocation source operation. Moreover, a noticeable effect of the strain rate is that a higher rate (10^{-2} s^{-1}) promotes the activation of basal slip within the $\{10\bar{1}2\}$ twin. While the twin nucleation occurs more easily at a high strain rate, here the twin growth rate cannot cope with the applied strain rate, so that strain energy accumulation increases with applied strain. When the twin grows to reach the required twin thickness for basal slip, the basal slip promptly activates within the twinned region to release the accumulated strain energy and plastic deformation swiftly catches up with the applied strain rate.

1. Introduction

As hexagonal-close packed (HCP) metals have a limited number of slip systems, deformation twinning plays a central role in deformation processes and leads to a more complicated deformation behavior compared to cubic metals [1,2]. In fact, the deformation of magnesium (Mg) is accommodated by twin- and slip-mediated deformation including tension or compression twinning as well as basal <*a*>, prismatic <*a*>, and pyramidal <*c*+*a*> slip [3]. A large difference in the activation energies between the available deformation modes at specific loading conditions often causes strongly anisotropic deformation behavior [4–6]. The deformation behavior becomes even more complicated at small-scales, as the geometrical constraints (grain boundaries or surfaces) additionally affect the activation of deformation modes, usually leading to "smaller is stronger" size effects and the transition of deformation modes at a critical size and specific dimension [7–11].

The $\{10\bar{1}2\}$ twinning mode of Mg has been studied extensively because of its frequent activation after basal slip at room temperature [12,13]. The $\{10\bar{1}2\}$ twinning cannot be achieved by the glide of partial dislocations as in face-centered cubic (FCC) metals because the twinning shear is 0.129 and the equivalent Burgers vector of a dislocation is only 0.025 nm [14,15]; A dislocation with such a small Burgers vector can hardly form and glide on the highly

* Corresponding author. Department of Energy Science, Sungkyunkwan University (SKKU), Suwon, 16419, Republic of Korea.
E-mail address: sanghooh@skku.edu (S.H. Oh).

https://doi.org/10.1016/j.actamat.2018.07.027

corrugated $\{10\bar{1}2\}$ twin plane with the interplanar spacing of 0.19 nm. The concept of a twinning dislocation has been proposed to support the shear-dominant twinning mechanism, which is a disconnection (a zonal dislocation) with a dislocation character with Burgers vector **b** and a step character with height **t** [16–18]. As the twin plane is not a slip plane where twinning dislocations can glide, the formation and glide of twinning dislocations on the $\{10\bar{1}2\}$ twin plane have been envisaged to involve non-planar dissociations of glissile dislocations in a pile-up array [19–21]. On the other hand, a number of molecular dynamic (MD) simulations have shown that the nucleation and growth of $\{10\bar{1}2\}$ twins can be achieved via pure atomic shuffling, without involving shear by the glide of twinning dislocations [14,22]. Apart from MD simulations recent transmission electron microscopy (TEM) investigations of the $\{10\bar{1}2\}$ twin contributed to understanding of the twinning mechanism. Detailed TEM observations discovered that most of the $\{10\bar{1}2\}$ twin boundaries (TBs) deviate from the ideal $\{10\bar{1}2\}$ twin plane orientation and consist of not only the coherent $\{10\bar{1}2\}$ twin plane, but also basal/prismatic (BP) and/or prismatic/basal (PB) interfaces [23–26]. Recent in-situ TEM deformation has further shown that the twin relationship can be attained by direct lattice reorientation through the transformation of basal to prismatic planes, and vice versa [27].

Apart from the twinning mechanism, size effects of twinning on the mechanical properties and deformation behavior of Mg have also been studied extensively. Most of the early studies have focused on microcompression of *c*-axis oriented single crystal Mg pillars. Lilleodden et al. [28] and Byer et al. [29,30] showed that the deformation of micropillars with 2–10 μm diameter occurs predominantly by pyramidal slip without deformation twinning. Yu et al. [31] performed in-situ TEM compression of a sub-micron Mg pillar and showed that it deforms predominantly by deformation twinning. Recently, microcompression of Mg $[2\bar{1}\bar{1}0]$ pillars has been conducted by Prasad et al. [32] and reported that the pillars deform by both slip and twinning modes. Sim et al. [10] performed microcompression of *a*-axis oriented Mg $[2\bar{1}\bar{1}0]$ pillars over a wide range of sizes from ~2 to 20 μm and showed that the deformation is dominated by nucleation and propagation of $\{10\bar{1}2\}$ twins. This twin-mediated deformation mode exhibited a strong size-dependent strengthening (size exponent $n = 0.77$), even stronger than that of typical dislocation slip (n ~0.6) [7]. In addition, the deformation mode showed a transition from the nucleation and propagation of multiple twins to single twin dominated mode as the size of pillar decreases below 18 μm. Accompanying MD simulations predicted another transition in deformation mode at a smaller size, i.e. a transition from twinning-mediated to dislocation-mediated plasticity at crystal sizes below a few hundred nanometers [10].

One notable size effect concerning deformation twinning in HCP metals is that it is suppressed when the crystal size falls below a certain limit, which is opposite to what is usually exhibited by FCC metals [33,34]. The experiments and MD simulations have shown that the nucleation stress of deformation twinning in HCP metals increases more steeply with decreasing size than that of dislocation slip, resulting in a transition of deformation mode at a critical size, below which dislocation slip is favored [8,10]. Thus, a question naturally arises as to why deformation twinning shows a stronger size effect than dislocation slip in HCP metals. To address this issue, one should understand the fundamental twinning mechanism and its relevance to the crystal size. Yu et al. [8] suggested that deformation twinning is not preferred at small sizes because the decreasing density of twin promoters, i.e. threading screw pole dislocations, decrease the probability of adjacent twin planes for the nucleation of twins. Sim et al. [10] proposed a model based on the size- and stress-dependent behavior of twin promoters, i.e. pre-existing prismatic <*a*> dislocations. While these pre-existing dislocations can act as local stress concentrators and promote twin nucleation in relatively large pillars where their glide is suppressed, in small pillars under high local shear stresses they become mobile and act as dislocation sources, favoring dislocation slip processes.

Furthermore, also the effect of strain rate on the deformation behavior of HCP metals is important as deformation twinning is a rate-dependent process. For example, in the case of Mg alloys, while the deformation is accommodated mainly by dislocation slip at low strain rates (10^{-3} s^{-1}), the volume fraction of deformation twins increases with increasing strain rate (10^{3} s^{-1}) [35,36]. Regarding the nucleation phenomena, it should be noted that small activation volumes for twinning lead to an increased strain rate dependency of the nucleation stress [37,38]. This suggests that a change of strain rate can cause a change in the deformation behavior of Mg pillars.

In the present study, we carried out in-situ microcompression of Mg $[2\bar{1}\bar{1}0]$ pillars in a scanning electron microscope (SEM) and TEM to investigate the related size and strain rate effects on deformation behavior. The $[2\bar{1}\bar{1}0]$ pillar orientation was chosen in the light of the Schmid factor and the critical resolved shear stress (CRSS) as prismatic <*a*> slip and $\{10\bar{1}2\}$ twinning slip are expected to compete or interplay at the corresponding loading condition [39]. The size of the pillars used for in-situ SEM microcompression was in the range of 0.5–4 μm, while the 500 nm-pillars were used for in-situ TEM microcompression, which are smaller than those previously studied by Sim et al. [10]. To address the rate dependency of the deformation behavior, strain rates were varied from 10^{-4} s^{-1} to 10^{-2} s^{-1}. We observed that the nucleation and growth of a single $\{10\bar{1}2\}$ twin variant dominates the deformation at such small length scales. The $\{10\bar{1}2\}$ twinning exhibits a relatively strong size effect regarding the twin nucleation stress ($n = 0.7$). The nucleation mechanism of the $\{10\bar{1}2\}$ twin assessed by in-situ TEM directly showed that the pile-up of prismatic <*a*> dislocations acts as local stress concentration for the twin nucleation. Detailed in-situ TEM observations revealed that the dissociation of prismatic <*a*> dislocations plays a critical role in twin nucleation. Based on these in-situ observations, we discuss the nucleation mechanism of $\{10\bar{1}2\}$ twinning, its size effects and rate dependency with respect to the competitive deformation by prismatic slip.

2. Experimental details

2.1. Fabrication of pillars by FIB

A high purity Mg single crystal (99.999%, Goodfellow Cambridge Ltd.) with the orientation accuracy better than 2% was used for the fabrication of Mg pillars. For in-situ SEM microcompression tests, a thin square slice was cut from the Mg crystal to expose the (0001) surface with one of the edges parallel to the $[2\bar{1}\bar{1}0]$ direction. This slice was then electrochemically etched in a solution of 5 mL HNO_3 + 95 mL ethanol to produce a wedge shape that saves the time for focused ion beam (FIB, Leo 1540 XB, Carl Zeiss, Oberkochen, Germany) milling. For the fabrication of a series of square pillars for in-situ SEM micro compression, FIB structuring was performed along the sharp edge of the slice by milling parallel to all sides and the top surface of each pillar. The strategy for pillar preparation is described in more detail by Moser et al. [40]. To study the size effects in mechanical properties and deformation behavior, pillars with sizes of 4 μm, 2 μm, 1 μm, and 0.5 μm in square edge were prepared. The aspect ratio was fixed to 1:3 for all specimens to prevent buckling during compression. The acceleration voltage of the Ga^{+} ion beam during FIB milling was 30 kV, and the ion beam current was decreased from 5 nA for coarse cuts to 10 pA for final polishing of the pillar surfaces. The orientation of the pillar axis was

determined by using electron backscatter diffraction (EBSD) as well as electron diffraction in TEM, both of which yielded a misorientation of $7 \pm 2^{\circ}$ from the intended $[2\bar{1}\bar{1}0]$ direction.

For in-situ TEM compression tests, a slightly different method was adopted for the fabrication of Mg pillars since the accessible range of sample size to the 200 kV electron beam is limited. A square plate with the top surface orientation of $(2\bar{1}\bar{1}0)$ was cut and polished to a mirror finish using a 20 nm diamond suspension. FIB (Helios NanoLab 450 S, FEI) processing was carried out in regions free from unwanted deformation twins originating from mechanical polishing. Thin lamellae were extracted from the plate by a conventional lift-out method, then cylindrical shaped pillars with a mid-height diameter of 500 nm were fabricated using a 30 kV Ga^{+} ion beam in annular milling mode. To access two different zone axis of the pillars for in-situ TEM experiments, two lamellae with either a $[2\bar{1}\bar{1}0]$ or a [0001] foil normal were prepared. Basal slip preferred Mg $[2\bar{1}\bar{1}2]$ pillar was also prepared for comparison of deformation behaviors. Low energy milling with 5 kV and 1 kV Ga^{+} ion beam were subsequently employed to reduce the surface damages [41]. The as-fabricated pillars had an aspect ratio of ~1:5 with a taper angle of ~3°. Before in-situ TEM compression the samples were annealed in-situ in the high vacuum (~10^{-5} Pa) of the TEM column (JEOL 2100 F, JEOL, Tokyo, Japan) operated at 200 kV to remove FIB-induced defects [42]. The pillars were first heated from 298 K to 353 K in 10 min. Subsequently, the temperature was increased in 20 K step up to 453 K after stabilizing for 10 min at each temperature.

2.2. In-situ SEM mechanical tests

In-situ microcompression of the square shaped pillars was performed in a field emission SEM (LEO 982, Carl Zeiss, Oberkochen, Germany). Two deformation systems were utilized, each of which is dedicated for specific load and size ranges. For the larger pillars (4 μm, 2 μm), a microindenter system (UNAT-SEM 1, Zwick GmbH & Co. KG, Ulm, Germany) was used, which has a maximum applicable force of 300 mN and a conical diamond tip with a flat end of 16 μm diameter. For the smaller pillars (1 μm, 0.5 μm), a Hysitron Picoindenter PI-85 (Bruker Corporation, Billerica, USA) with a maximum force of 13 mN and a 5 μm flat end diamond punch was used. The diamond tips for both systems were provided by Synton MDP (Nidau, Switzerland). The in-situ SEM microcompression tests were performed in displacement controlled mode at nominal strain rate of 10^{-3} s^{-1}. Before the mechanical tests, the stiffness of the individual lamella was determined for the compliance correction. During the tests SEM images were captured with a frame grabber at a repetition rate of 1 frame per second and used for image analysis, sink-in correction, and local strain analysis later on. After the tests, EBSD analysis was performed on deformed pillars to measure the crystal rotations associated with deformation twinning.

2.3. In-situ TEM compression tests

In-situ TEM compression was conducted on the annealed pillars using a TEM nanoindentation holder (TEM-indenter, Nanofactory, Gothenberg, Sweden) equipped with a flat diamond punch in the field emission TEM (JEM-2100 F, JEOL, Tokyo, Japan). The compressive deformation was carried out in displacement controlled mode at strain rates ranging from 10^{-4} to 10^{-2} s^{-1}. To record the dynamic deformation processes, real-time TEM movies were recorded using a charge coupled device (CCD) camera (ORIUS 200D, Gatan, Pleasanton, USA) at 25 frames per second. Real-time TEM movies were recorded in dark-field (DF) imaging mode to enhance the defect contrast by selecting the $(\bar{2}111)$ and the $(\bar{1}100)$ diffraction spots for the pillars with the $[01\bar{1}0]$ and the [0001] zone axis orientations, respectively.

2.4. TEM orientation mapping of twins

Detailed TEM orientation mapping was performed to investigate the orientation changes associated with twinning. Hereby, the automated crystal orientation mapping system (ASTAR, NanoMEGAS, Brussels, Belgium) was used for the collection of electron diffraction patterns, data processing and image analysis. The diffraction patterns were recorded by a high-speed stingray CCD camera and compared with theoretically generated patterns using the template matching process. A condenser aperture with 50 μm in diameter was used to reduce the convergence angle of the beam, and a camera length of 25 cm was applied for all diffraction patterns with a scanning step size of 1 nm. To improve the accuracy of orientation mapping a precession angle of 0.5° was used as it produces more diffraction spots with reduced effects of dynamical diffraction [43].

3. Results

3.1. Deformation modes of Mg $[2\bar{1}\bar{1}0]$ pillars under compression

Possible deformation modes of Mg $[2\bar{1}\bar{1}0]$ pillar under compression are summarized in Table 1. For each mode the CRSS reported in literature and the Schmid factors (m) are given to predict a preferred deformation mode [44–52]. For basal <a> slip, although the CRSS is only ~1 MPa, the Schmid factor is zero. Therefore, basal <a> slip is not considered as a preferred deformation mode if the applied stress is uniaxial and uniform. Pyramidal <$c + a$> slip has the highest Schmid factor (0.45), but requires the highest CRSS (80 MPa). Prismatic slip has a high Schmid factor of 0.43, but the CRSS (39–50 MPa) is much higher than that of the competing $\{10\bar{1}2\}$ twin. CRSS and m for the $\{10\bar{1}2\}$ twin are 12 MPa and 0.37, respectively. As a first order estimate, the applied stress required to activate of each mode, CRSS/m is also provided for comparison. The CRSS/m for pyramidal slip, prismatic slip and $\{10\bar{1}2\}$ twin is ~178, 91–116, and 32 MPa, respectively. Thus, the $\{10\bar{1}2\}$ twin is expected to activate most easily when the Mg $[2\bar{1}\bar{1}0]$ pillar is compressed. It is noted that there are four twin variants with the same Schmid factor (0.37) among the total six (Table 1). It should be further noted that when the $\{10\bar{1}2\}$ twin forms, the compression axis within the twinned region is changed to the $[11\bar{2}3]$ as a consequence of twin-induced crystal reorientation [53]. The activation of basal slip is then preferred within the twin because of the high Schmid factor and the low CRSS.

3.2. Size effects on strength and deformation behavior

Fig. 1 shows a summary of typical in-situ SEM microcompression results obtained from a 4 μm pillar (Supplementary Video S1). The deformation behavior is characterized by a series of discrete load drops and concurrent strain bursts in the stress-strain curve (Fig. 1a). The first load drop occurred with the onset of yield after elastic loading, which is followed by a large displacement (Fig. 1b and c). The in-situ SEM image recorded at this event (Fig. 1c, shown in more detail in the inset) shows a slight tilt in the pillar edge orientation. During the subsequent deformation the stress level was maintained constant at ~125 MPa and the tilted feature propagated downwards until eventually a slip step formed along an inclined plane (white arrow in Fig. 1d) at a strain of ~6.5%. The later stage of deformation is then localized at this slip step with a slight extent of strain hardening. Another load drop occurred, accompanied by the appearance of a second tilted feature along the

Table 1
Schmid factor, CRSS and Peierls stress of the slip and twin systems considered for the compression of Mg $[2\bar{1}\bar{1}0]$ pillar.

Deformation mode		Schmid factor (m)		CRSS (MPa)	Peierls stress (MPa)		CRSS/m (MPa)	
		$[2\bar{1}\bar{1}0]$	$[11\bar{2}3]^*$		Edge	Screw	$[2\bar{1}\bar{1}0]$	$[11\bar{2}3]^*$
Basal $\langle a\rangle$	$(0001)[11\bar{2}0]$	0	0.45	0.81 [44]	0.3 [45]	3.6 [45]	–	1–2
	$(0001)[1\bar{2}10]$	0	0.22	0.76 [46]				
	$(0001)[\bar{2}110]$	0	0.22	0.52 [47]				
Prismatic $\langle a\rangle$	$(1\bar{1}00)[11\bar{2}0]$	0.43	0	39 [48]	13 [45]	44 [45]	91–116	325-417
	$(10\bar{1}0)[1\bar{2}10]$	0.43	0.12	50 [49]				
	$(01\bar{1}0)[\bar{2}110]$	0	0.12					
Pyramidal II $\langle c+a\rangle$	$(11\bar{2}2)[\bar{1}\bar{1}23]$	0.11	0.0	80 [50]	208 [51]	157 [51]	178	200
	$(\bar{1}2\bar{1}2)[1\bar{2}13]$	0.11	0.39					
	$(\bar{2}112)[2\bar{1}\bar{1}3]$	0.45	0.19					
	$(\bar{1}\bar{1}22)[11\bar{2}3]$	0.11	0					
	$(1\bar{2}12)[\bar{1}2\bar{1}3]$	0.11	0.19					
	$(2\bar{1}\bar{1}2)[\bar{2}113]$	0.45	0.39					
$\{10\bar{1}2\}$twin	$(10\bar{1}2)[\bar{1}011]$	0.37	0.23	12 [52]	–	–	32	33
	$(\bar{1}012)[10\bar{1}1]$	0.37	0.28					
	$(\bar{1}102)[1\bar{1}01]$	0.37	0.36					
	$(1\bar{1}02)[\bar{1}101]$	0.37	0.36					
	$(0\bar{1}12)[01\bar{1}1]$	0	0.28					
	$(01\bar{1}2)[0\bar{1}11]$	0	0.23					

*Due to the crystal reorientation in $\{10\bar{1}2\}$-twinned region, the loading axis is changed from $[2\bar{1}\bar{1}0]$ to $[11\bar{2}3]$.

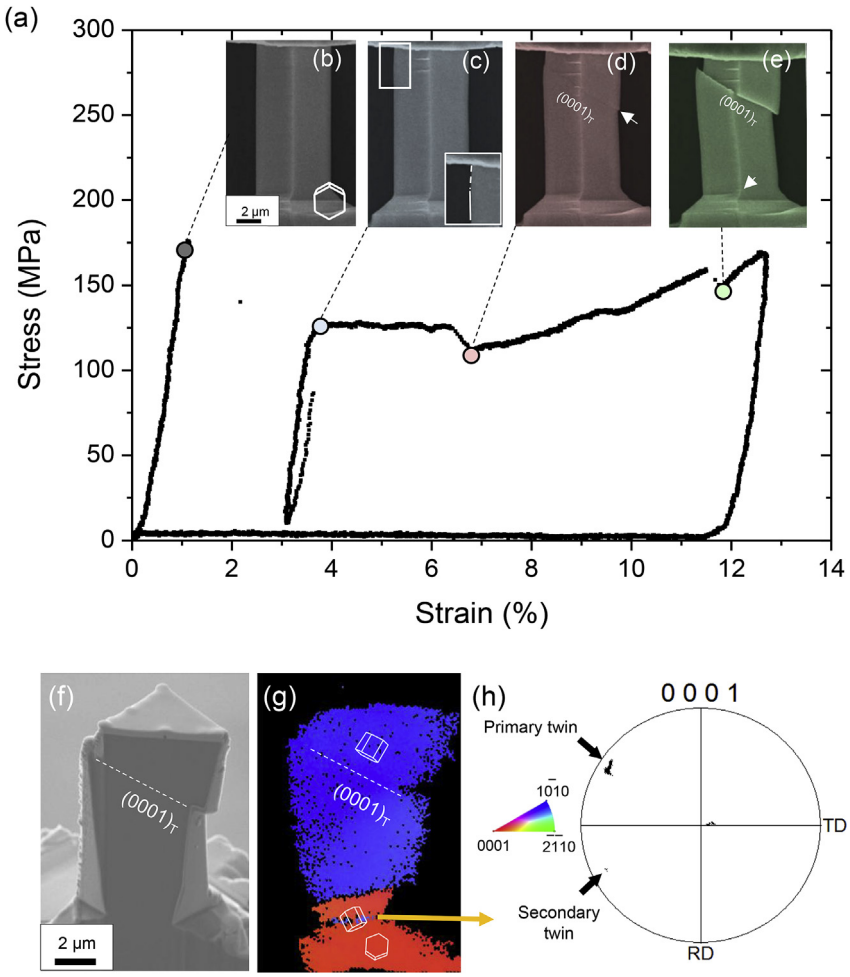

Fig. 1. In-situ SEM microcompression results of a 4 μm Mg $[2\bar{1}\bar{1}0]$ pillar at a strain rate of 10^{-3} s^{-1}. (a) Stress-strain curve. (b–e) SEM images corresponding to the positions marked on the stress-strain curve. In specific, (b) before onset of plastic deformation ($\varepsilon = 1.1\%$); (c) after the large load drop ($\varepsilon = 3.7\%$) showing a tilt of the sample edge due to $\{10\bar{1}2\}$ twining; (d) formation of a slip line along the $(0001)_T$ basal plane (white arrow) within the twinned region ($\varepsilon = 6.5\%$); (e) activation of the secondary twin at the base of pillar (white arrow) ($\varepsilon = 11.5\%$). The in-situ SEM movie with correlated stress-strain curve is provided as Supplementary Movie S1. (f) Cross-section of the deformed pillar prepared by FIB. (g) EBSD orientation map of the cross-section. (h) EBSD (0001) pole figure showing the formation of two $\{10\bar{1}2\}$ twin variants indicated as primary and secondary twins.

edge orientation near the bottom of the pillar (white arrow in Fig. 1e) at a strain of 11.5%, when the stress had risen back up to about the yield stress.

Supplementary videos related to this article can be found at https://doi.org/10.1016/j.actamat.2018.07.027.

EBSD analysis of the deformed pillar (Fig. 1f and g) showed that the crystal orientation of the whole pillar was changed by ~90° from the original orientation, confirming the crystal reorientation induced by $\{10\bar{1}2\}$ twinning. Thus, the initial load drop accompanied by the change of sample edge geometry is due to the nucleation of a $\{10\bar{1}2\}$ twin and the associated crystal reorientation, succeeded by twin thickening at a rather constant stress. It becomes evident that the slip step was formed along the basal plane within the twinned region, which is indexed as the $(0001)_T$. As already discussed in section 3.1, basal slip is preferred in the twinned region because of the crystal reorientation of the pillar axis from the $[2\bar{1}\bar{1}0]$ to the $[11\bar{2}3]$ (Table 1). In section 3.4 we will further show that basal slip can initiate either during twin propagation or after its full propagation throughout the pillar, which essentially depends on the applied strain rate. The EBSD map also shows the formation of a conjugate twin near the bottom mount of the pillar, which corresponds to the second load drop at the strain of 11.5% (Fig. 1e, g, h). Note that the stress at which the secondary twin forms is similar to that of the primary twin.

Fig. 2 shows stress-strain curves of pillars with different sizes ranging from 4 μm to 0.5 μm tested at a strain rate of 10^{-3} s^{-1}. Regardless of the pillar size, all stress-strain curves exhibited a pronounced load drop at the onset of yield, which is associated with the formation of a $\{10\bar{1}2\}$ twin. Notably, as the pillar size decreases the yield stress increases, but the amount of strain occurring in the burst event decreases (this might, however, be to some extent affected by the machine dynamics during the displacement controlled experiments). Representative SEM images of the deformed pillars are shown as inset for each pillar size. They clearly depict the formation of large single slip step along the $(0001)_T$ orientation for all deformed pillars, indicating that basal slip was activated within the twinned region and dominated the rest of deformation. The in-situ SEM microcompression results suggest that the deformation characteristics of the pillars, i.e. initial $\{10\bar{1}2\}$ twinning followed by basal slip in the twinned region, are the same for all pillars tested at the strain rate of 10^{-3} s^{-1}.

To evaluate the size effects on $\{10\bar{1}2\}$ twinning, the yield stress at which twin nucleation commences and the flow stress for twin propagation were plotted as a function of pillar size in Fig. 3a and b, respectively. We define the nucleation stress (σ_N) as the peak stress prior to the first load drop, and the propagation stress (σ_P) as the 1% offset stress after the first strain burst associated with twin nucleation. The size exponent (n) for the nucleation and the propagation stress assuming a power law is evaluated to be 0.70 ± 0.20 and 0.47 ± 0.07, respectively, indicating that the nucleation stress varies much more sensitively with size than the propagation stress.

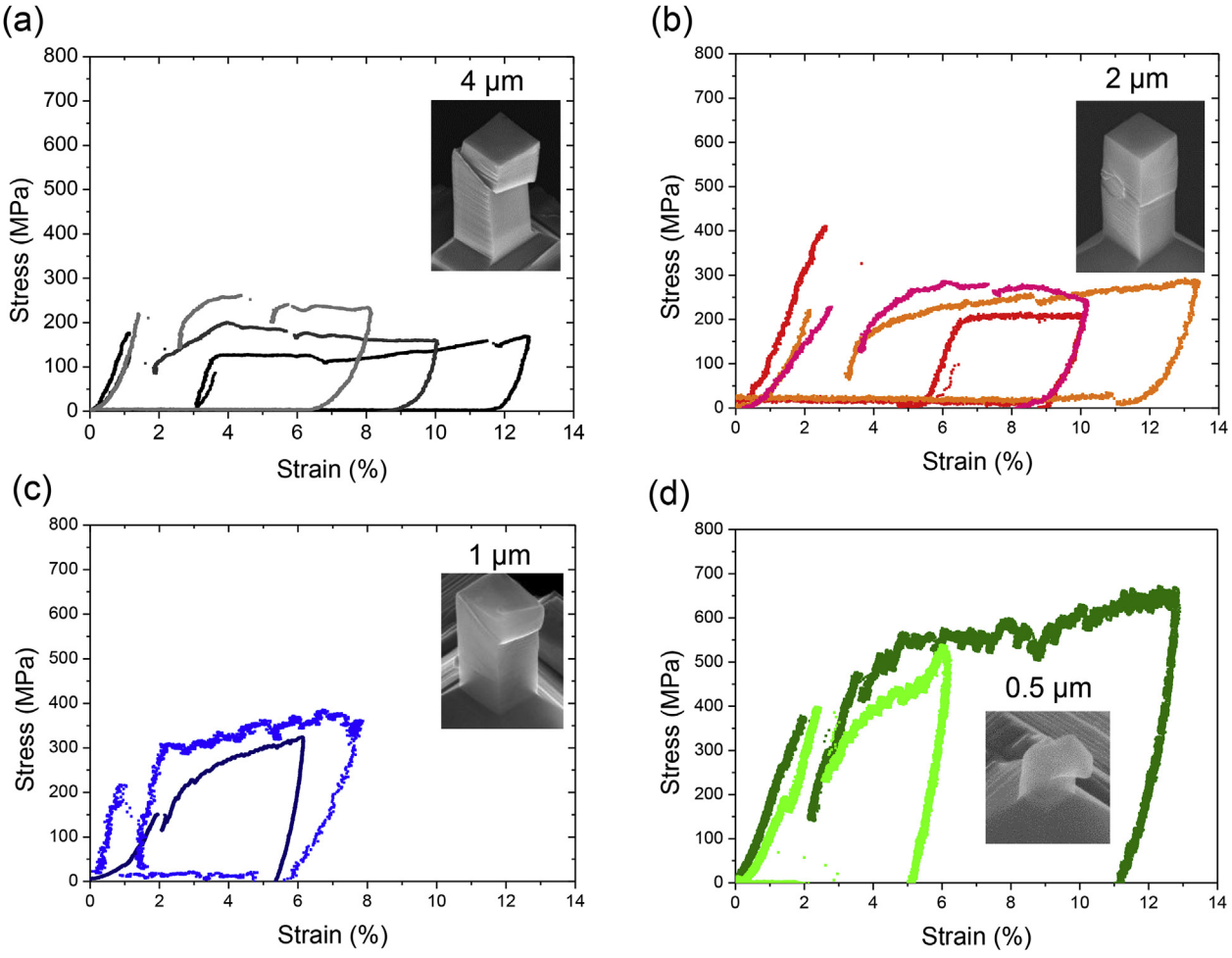

Fig. 2. Stress-strain curves of Mg $[2\bar{1}\bar{1}0]$ pillars with sizes of (a) 4 μm; (b) 2 μm; (c) 1 μm; (d) 0.5 μm. A representative SEM image of deformed pillar is shown for each size as inset.

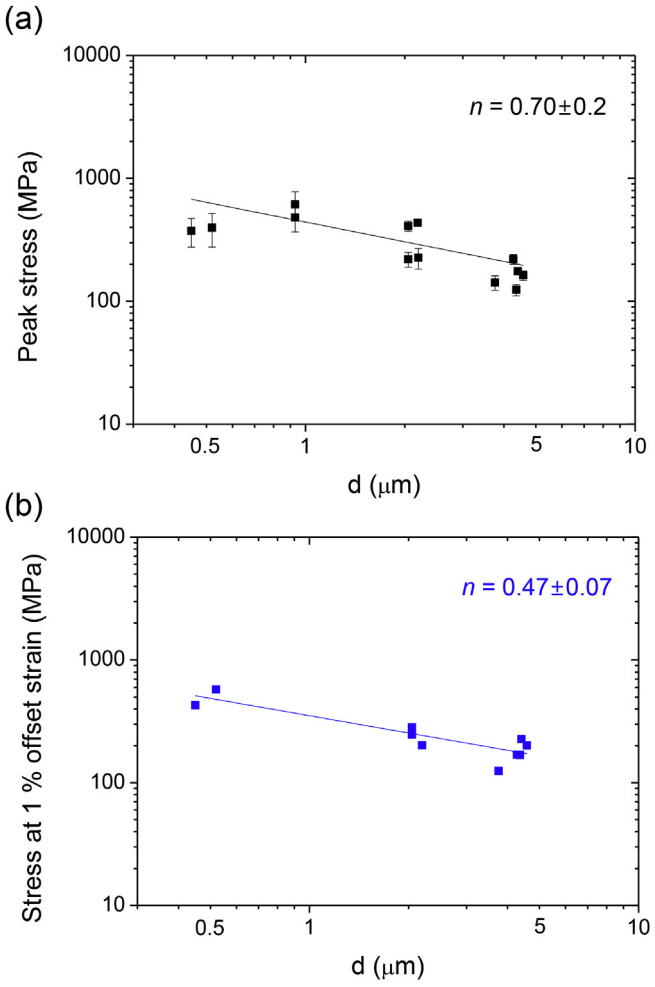

Fig. 3. Stress vs. size plot of Mg [$2\bar{1}\bar{1}0$] pillars. (a) The peak stress measured before the first apparent load drop, which is attributable to the twin nucleation stress (σ_N). (b) Stress measured at 1% offset strain after the load drop, which is associated with the twin propagation stress (σ_P). The data points were fitted by $\sigma = d^{-n}$ to determine the size exponent (n), which yields (a) $n = 0.70 \pm 0.20$ and (b) 0.47 ± 0.07, respectively.

3.3. Nucleation and growth of {$10\bar{1}2$} twin

Typical SEM and TEM images of an as-FIB-prepared pillar are shown in Fig. 4a and b. The as-FIB-prepared pillar contains a lot of structural defects such as dislocation loops and debris which were formed by the high energy Ga^+ ion beam bombardment. After the annealing up to 453 K, the dislocation density dropped significantly as seen in Fig. 4c. The measurement of dislocation density using the line intersection method yields an average density on the order of 10^{13} m^{-2}.

Fig. 5 shows a series of TEM snapshot images representing the overall deformation behavior of the [$2\bar{1}\bar{1}0$] Mg pillar. Plastic deformation begins with the appearance of local strain contours under the contact (Fig. 5b), where complex dislocation processes involving nucleation, pile-up, cross slip and dissociation reactions occurring on prismatic as well as basal planes (Fig. 5c and d). We point out that these dislocation processes are commonly observed before {$10\bar{1}2$} twinning in all tested pillars and they apparently act as precursors for the formation of a stable twin nucleus (refer to Supplementary Movie S2, S3, and S4). In fact, a stable twin nucleus appeared at the dislocation junction (white arrow in Fig. 5d) and then propagated laterally to create a lenticular twin lamella (Fig. 5e). Once it spanned the whole sample, it thickened by

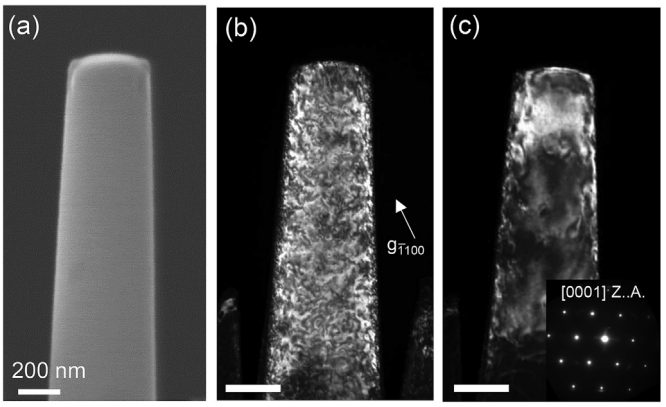

Fig. 4. (a) SEM image of an as-FIB-prepared 0.5 μm Mg [$2\bar{1}\bar{1}0$] pillar for in-situ TEM. (b) TEM DF image of the as-FIB-prepared Mg pillar. The TEM image shows a high density of FIB-induced defects. (c) TEM DF image of the same pillar after annealing inside the TEM up to 453 K. The FIB-induced defects were effectively annealed out. The dislocation density of the annealed pillar is ~1.1×10^{13} m^{-2}.

(downward) migration of the TB throughout the pillar (Fig. 5f), dominating the deformation of the sample (refer to Supplementary Movie S2, S3, and S4). The diffraction pattern obtained along the [$11\bar{2}0$] zone axis after deformation reveals the {$10\bar{1}2$} twin relationship between matrix and twin (Fig. 5g). While the deformation twinning is governed by the nucleation and growth of a single {$10\bar{1}2$} twin variant, the later stage of deformation is carried either by the activation of conjugate twin variants or basal slip within the twinned region, since the axial strain that can be accommodated by the full propagation of a single twin variant along the pillar is limited (~6.5%) [25].

The elemental processes governing the aforementioned twinning behavior are analyzed in more detail based on the frame analysis of in-situ TEM movies in the following figures (Figs. 6–10), focusing on pre-nucleation dislocation activities (Figs. 6–8), twin nucleation (Fig. 9), and twin growth (Fig. 10). The first dislocation activity in the Mg pillars is the nucleation of half-loops at the contact with the punch. In fact, this pillar-punch contact provides preferential nucleation sites for dislocations as the local stress is high due to the tapering of the pillar and the roughness of the punch surface. All tested Mg pillars with various orientaions in our research showed the initial deformation taking place at the contact, independent of pillar orientation (data not shown). Then, as shown in Fig. 6a for a basal slip preferred [$2\bar{1}\bar{1}2$] pillar, the nucleated dislocations glide down along the respective slip system to escape, interact or multiply (Supplementary Movie S5). In the case of the [$2\bar{1}\bar{1}0$] pillar, however, the glide of nucleated dislocations is restricted to only a short distance (Fig. 6b), which is quite different from the basal slip in the [$2\bar{1}\bar{1}2$] pillar. Considering the line shape of the half-loops and the geometry of slip systems, these dislocations are most likely prismatic <a> dislocations lying on an inclined ($\bar{1}010$) prismatic plane. Considering the high Schmid factor (Table 1), the activation of prismatic slip is in principle possible once a local resolved shear stress exceeds the CRSS. These dislocations, with their arms being pinned at the contact and the central line portion being dragged over some distance, bow out into half-loops but could not extend the line length any further (Fig. 7 and Supplementary Movie S6). It appears that the two arms of half loops with screw character have relatively low mobility, in contrast to the central portion with edge character (refer to Table 1). As the glide or source operation is limited by seemingly different mobility of screw and edge characters, the half-loop dislocations are piled up and thus the region in front of the pile-up becomes highly stressed, exhibiting highly localized strain field contrast (see the onion shell-

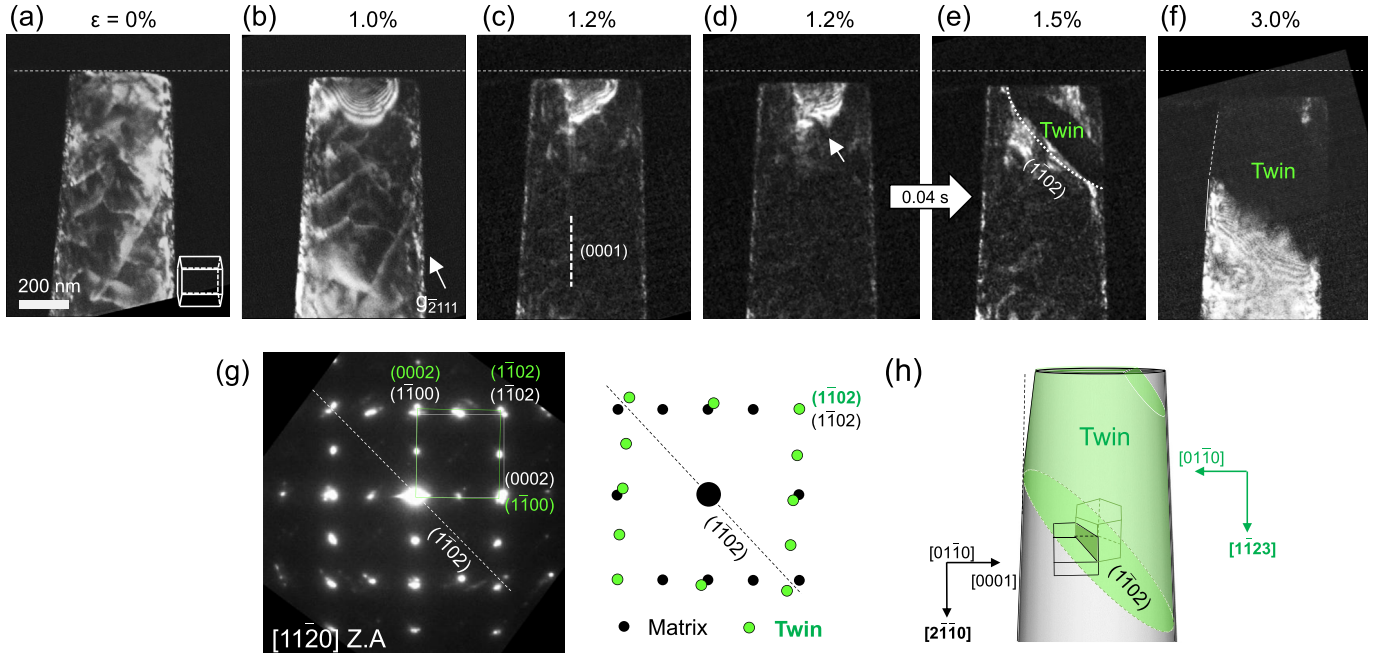

Fig. 5. A series of in-situ TEM images highlighting key steps in the formation of a $\{10\bar{1}2\}$ twin. (a) Before compression ($\varepsilon = 0\%$); (b) Evolution of local strain contrast emanating from the contact at the initial stage of deformation ($\varepsilon = 1.0\%$); (c) Stacking faults emerging from the strain contrast along the (0001) plane ($\varepsilon = 1.2\%$); (d) Formation of a $\{10\bar{1}2\}$ twin nucleus at the dislocation junction (white arrow, $\varepsilon = 1.2\%$); (e) Propagation of the twin tips ($\varepsilon = 1.5\%$). Within 0.04 s the propagation was completed, resulting in the formation of a twin lamella. (f) Thickening of the twin by migration of TBs. Note that the TB is inclined along the $[01\bar{1}0]$ viewing direction. The strain rate was 10^{-4} s^{-1}. The corresponding in-situ TEM movie is provided as Supplementary Movie S2 (Pillar 1). (g) A $[11\bar{2}0]$ zone axis electron diffraction pattern showing the $(1\bar{1}02)$ twin relationship between matrix and twin. (h) Schematics indicating the orientaion of the $(1\bar{1}02)$ twin plane and the crystal reorientation associated with the twinning.

like strain contours in Fig. 7c and d. With an increase of applied strain the strain contours extend further, revealing dislocation line contrast inside this strained zone.

During further loading straight line defects suddenly emerged from the dislocation pile-up (Fig. 8 and Supplementary Movie S6). The fact that these line defects initiate near the screw component and move along the basal plane suggests that the screw component of the prismatic <*a*> dislocations cross-slipped to the (0001) basal plane. The prismatic-to-basal cross slip of <*a*> dislocation, and vice versa, is in principle possible, as the screw component can glide on both $(\bar{1}010)$ prismatic and (0001) basal planes, and has also been experimentally observed [54]. The extending straight line contrast along the basal plane indicates the formation of stacking faults (SF), implying that the dislocation was dissociated after cross slip, one of which glides on the basal plan and leaves a SF behind. As the stress increased in the dislocation pile-up during further loading, several more cross-slip and glide events occurred from the other ends of half-loops, resulting in the formation of a series of parallel SF ribbons (White arrows in Fig. 8a).

After formation of SFs along the basal planes, the $\{10\bar{1}2\}$ twinning occurred suddenly at the junction of prismatic <*a*> dislocations and basal SFs (Fig. 9a and b and Supplementary Movie S7). Although the detailed mechanism of twin nucleation cannot be assessed as it occurred too fast (the time interval between two frame images is only 0.04 s, within which the twin already nucleated and propagated over a distance, see e.g. Fig. 9b), the present in-situ TEM observations show that the heterogeneous nucleation of a twin nucleus can be induced by high local stress at the defect site such as dislocation pile-up, and the prior dislocation processes taking place on the $(\bar{1}010)$ prismatic and the (0001) basal planes play an important role in the nucleation of $\{10\bar{1}2\}$ twin by acting as a precursor to the formation of a stable twin nucleus (Fig. 9a).

Once a twin nucleates, further deformation is governed by its thickening (Fig. 10 and Supplementary Movie S7). This occurred by migration of TBs along both upward and downward directions, but more dominantly along the downward direction (Fig. 10a and b). In addition, there was a transition in the morphology of the moving TB from a sharp lenticular to a wavy and diffuse shape, implying that the latter one consists of lattice planes with different orientations. Furthermore, a diffraction contrast associated with the strain fields of dislocations was observed ahead of the moving TB. This indicates that there must be local dislocation activities in front of the TB to assist the twinning.

3.4. Rate-dependent deformation behavior

As shown before, the $\{10\bar{1}2\}$ twinning is a dominant deformation mode of Mg $[2\bar{1}\bar{1}0]$ pillars under compression at the applied strain rate of 10^{-3} s^{-1}. A noticeable rate effect is that a higher strain rate promotes the nucleation of twins at a lower applied strain. For example, at the high strain rate of 10^{-2} s^{-1} the nucleation of twinning was activated at a lower strain with less prior dislocation activity (Fig. 11, Supplementary Movie S4 and S11). A twin nucleated suddenly in the upper part of the pillar, as evident from the change in diffraction contrast (Fig. 11b), followed by twin thickening through downward propagation of the TB (Fig. 11c). The diffraction pattern analysis (Fig. 11f) and orientation mapping after deformation (Fig. 11g) confirmed that the contrast change was related to $\{10\bar{1}2\}$ twinning. However, during twin thickening, basal slip was activated suddenly within the twinned region and dominated the rest of deformation (white arrow in Fig. 11c and d; Supplementary Movie S11). This deformation behavior is different from the case of the strain rate of 10^{-3} s^{-1}, where the primary twin extends all the way to the base of pillar until the whole pillar is reoriented before basal slip is activated (see for example Fig. 1f and g and Supplementary Movie S3). The in-situ TEM observation

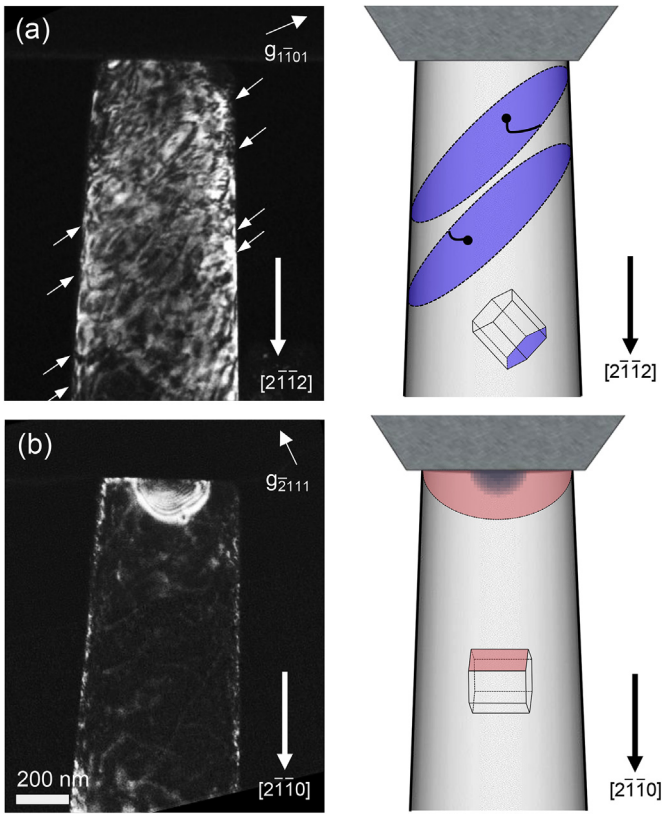

Fig. 6. TEM images and schematics representing the difference between basal <*a*> and prismatic <*a*> slip in the $[2\bar{1}\bar{1}2]$ and the $[2\bar{1}\bar{1}0]$ pillars during compression, respectively. (a) Mg $[2\bar{1}\bar{1}2]$ pillar, where the basal plane is oriented favorable for dislocation slip. Several single-armed sources are activated, leading to local basal <*a*> slip. The corresponding in-situ TEM movie is provided as Supplementary Movie S5. (b) Mg $[2\bar{1}\bar{1}0]$ pillar, where the prismatic plane is oriented favorable for dislocation slip (the pillar of interest in this paper). Different from the easy activation of basal slip in the Mg $[2\bar{1}\bar{1}2]$ pillar, dislocaton half-loops emanating from a source in the Mg $[2\bar{1}\bar{1}0]$ pillar are non-glissile, leading to the formation of a strongly localized strain contour (refer to Fig. 7).

shows that at the high strain rate basal slip is activated once the twin thickness required for the unimpeded extension of basal slip across the pillar is reached by twin thickening. According to the in-situ TEM observation, the measured twin thickness before basal slip is ~520 nm or ~21% of the pillar length, which correspond to an axial strain of 1.40% (Fig. 11c).

On the contrary, at the low strain rate of 10^{-4} s^{-1} extensive prior dislocation activities, mostly prismatic slip with sporadic activation of basal slip along the axial direction, were observed up to 1% strain before the twin nucleation commenced. Fig. 12 shows the in-situ TEM microcompression results of $[2\bar{1}\bar{1}0]$ Mg pillar perfomed at the strain rate of 10^{-4} s^{-1} with the [0001] zone axis orientation, which provides a full plan-view of the basal plane but an edge-on view of the prismatic slip plane (Supplementary Movie S8). Although the deformation behavior is slightly different from the previous cases due to the lower strain rate, the in-situ TEM confirmed that the initial deformation is dominated by prismatic <*a*> slip (Fig. 12b). Note that the prismatic <*a*> slip occurs under a symmetric double slip configuration and results in a uniform distribution of dislocations in the pillar. The dislocation density, however, remains only high close to the contact, as the dislocations could not glide further down or escape through the side surfaces, in agreement with previous observations along the $[01\bar{1}0]$ direction (Fig. 7). With proceeding deformation, a weak dislocation line contrast followed by fuzzy and diffusive diffraction contrast spanning the whole pillar width moved down. Later, a clear line contrast of dislocations (perfect dislocation) was observed more dominantly along the same direction (White arrows in Fig. 12c). Considering the slip plane geometry and slip distances, these dislocations must be gliding on the basal planes and relate to the formation of basal SFs as shown in Fig. 8. Up to this point, there was no contrast change or additional diffraction spots in the electron diffraction pattern indicating the formation of a twin (Fig. 12d). Consequently, the initial deformation before the nucleation of $\{10\bar{1}2\}$ twin is accommodated by prismatic and basal slip.

The axial strain accommodated by prismatic slip, $\{10\bar{1}2\}$ twinning and basal slip at the different strain rates (10^{-4}, 10^{-3} and 10^{-2} s^{-1}) was measured and plotted with deformation time in Fig. 13. The applied strain is drawn as a line in each plot for comparison. The strain was measured from in-situ TEM movies at the corresponding time steps. It is evident that for the low rate deformation (10^{-4} ~ 10^{-3} s^{-1}) the initial dislocation slip and $\{10\bar{1}2\}$ twinning can effectively accommodate the imposed strain at any given time, so that the accumulation of strain energy is not so significant (Supplementary Movie S9, S10). For the high strain rate

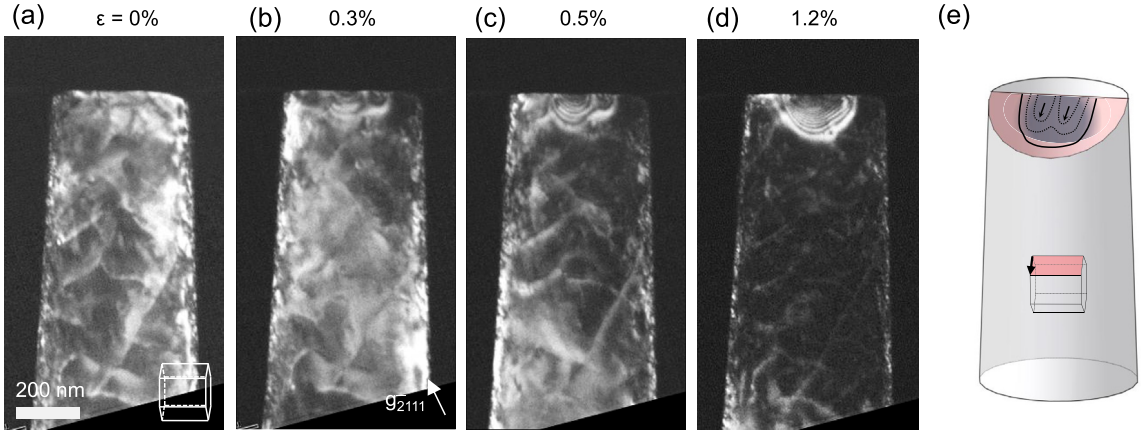

Fig. 7. TEM images showing the detailed process of the strain contour evolution associated with dislocation source activation. (a) Before deformation and (b–d) development of a local strain contour during compression. Dislocation half-loops were nucleated and bowed out with their arms being pinned at the contact (onion shell-like strain contours in (c) and (d)). The corresponding in-situ TEM movie is provided as Supplementary Movie S6. (e) Schematic showing that the glide of dislocation half-loops within the strain contour is limited due to the low mobility of screw component (Table 1).

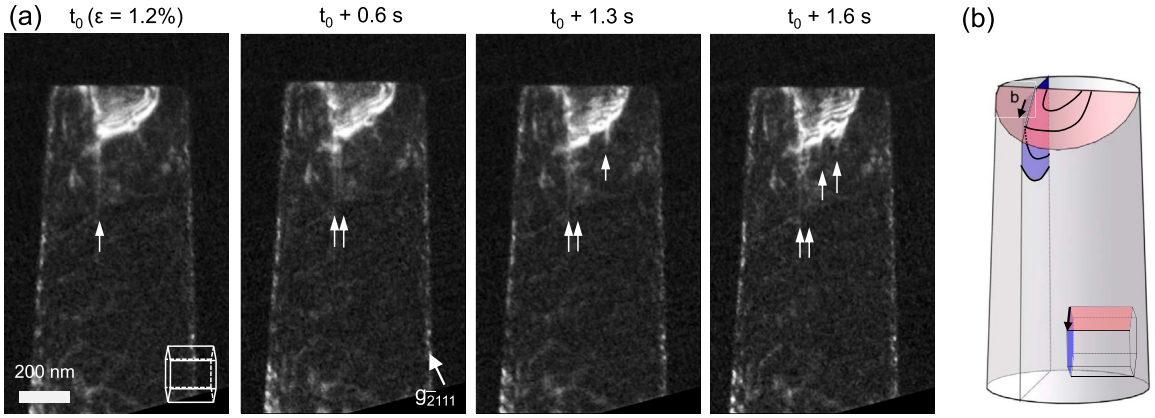

Fig. 8. Detailed process of the activation of basal slip from the pile-up of prismatic <*a*> dislocations. (a) The straight line contrast running along the basal plane indicates the formation of a stacking fault (SF) (white arrows). A series of parallel SFs running on basal planes is likely to form by cross-slip and subsequent dissociation of the screw component of the half-loop shaped prismatic <*a*> dislocations. The corresponding in-situ TEM movie is provided as Supplementary Movie S6. (b) Schematic model illustrating the in-situ TEM observation.

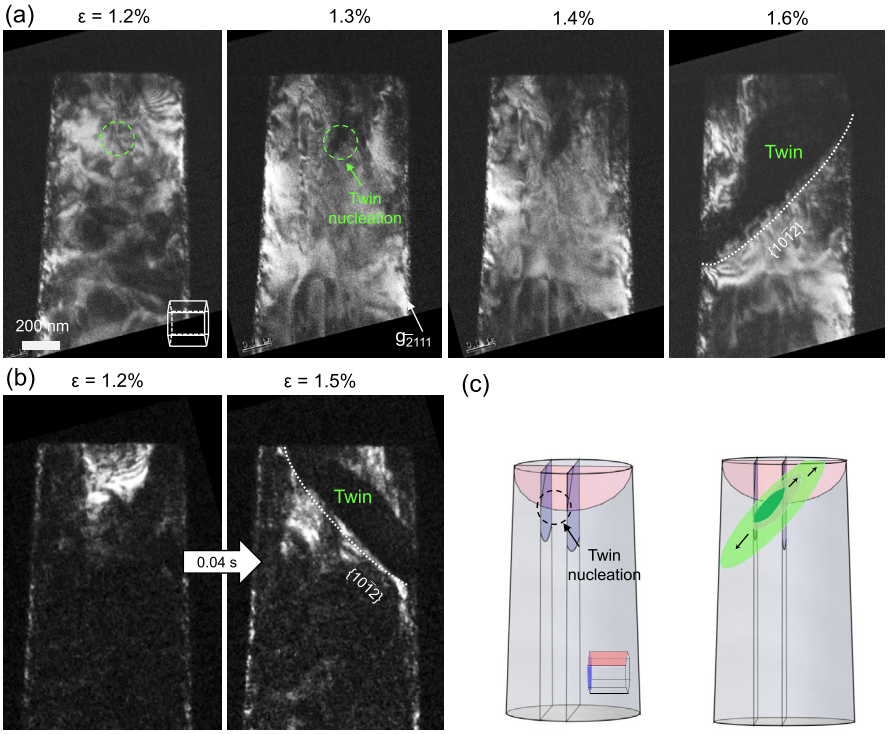

Fig. 9. TEM snapshots showing the detailed process of twin nucleation and propagation. (a) Nucleation of a twin at the junction between prismatic <*a*> dislocation and basal SFs (indicated by a green circle), followed by twin propagation and thickening. (b) Sudden nucleation and subsequent propagation of a twin observed from another pillar. Note that different twin variants with the same Schmid factor have been ativated in the pillars shown in (a) and (b) (refer to Table 1). The corresponding in-situ TEM movie is provided as Supplementary Movie S7. (c) Schematic illustration showing the nucleation and propagation of a twin at the dislocation junction. (For interpretation of the references to color in this figure legend, the reader is referred to the Web version of this article.)

deformation (10^{-2} s^{-1}), as the axial strain produced by propagation of the $\{10\bar{1}2\}$ twin is not sufficient to accommodate the applied strain at a given time, the strain energy accumulates and increases with applied strain (Supplementary Movie S11). When the twin grows to reach the required twin thickness for basal slip, basal slip promptly activates to release the accumulated strain energy and swiftly catches up to the applied strain (Fig. 13c). Although favored by the Schmid factor, the activation of basal slip within the $\{10\bar{1}2\}$ twin competes with the twin growth and is determined by the strain energy accumulated within the twin as a consequence of the rate-limiting strain release by twin growth.

4. Discussion

4.1. Nucleation and growth mechanisms of the $\{10\bar{1}2\}$ twin

Twinning occurs heterogeneously at locations of high stress concentration. Grain boundaries (GBs) are usually one of the most preferential sites for the nucleation of twins in bulk Mg [22,55–57]. Single crystal Mg pillars, in the absence of preexisting GBs and TBs, require an alternative source for twin nucleation. Our in-situ TEM directly shows that it is dislocation pile-up that provides local stress concentration for twin nucleation in the Mg $[2\bar{1}\bar{1}0]$ pillars.

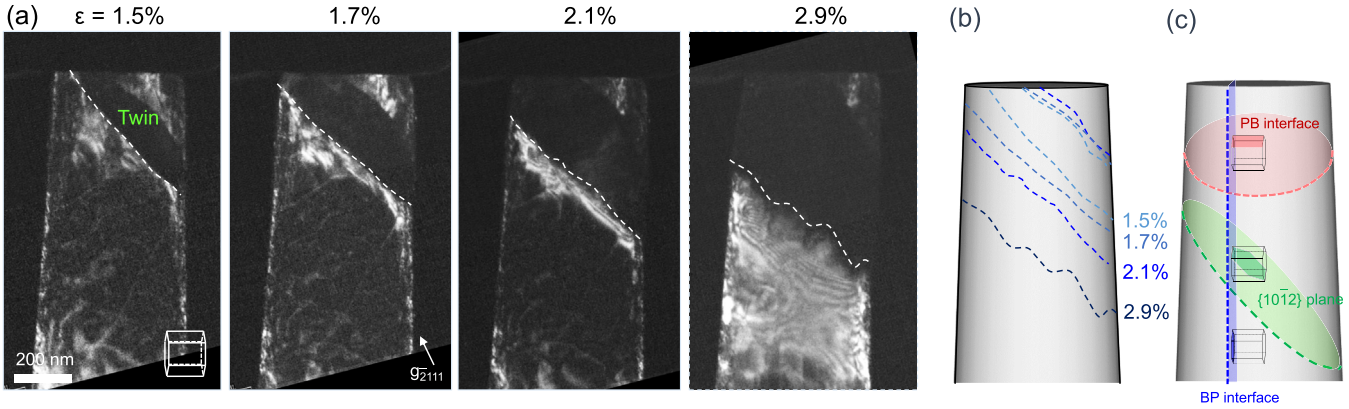

Fig. 10. Detailed TEM observations of twin thickening. (a) A series of TEM images showing the roughening of the twin boundary (TB) during migration. Pronouncing diffraction contrast associated with strain and/or dislocations is observed ahead of the moving TB. (b) Schematic showing the trace of the TBs during migration. The orientation of the moving TBs deviates gradually from the {10$\bar{1}$2} twin plane. The corresponding in-situ TEM movie is provided as Supplementary Movie S7. (c) Schematic showing the {10$\bar{1}$2} twin plane, basal-prismatic (BP) and prismatic-basal (PB) matrix-twin interfaces to guide the orientation of the moving TB.

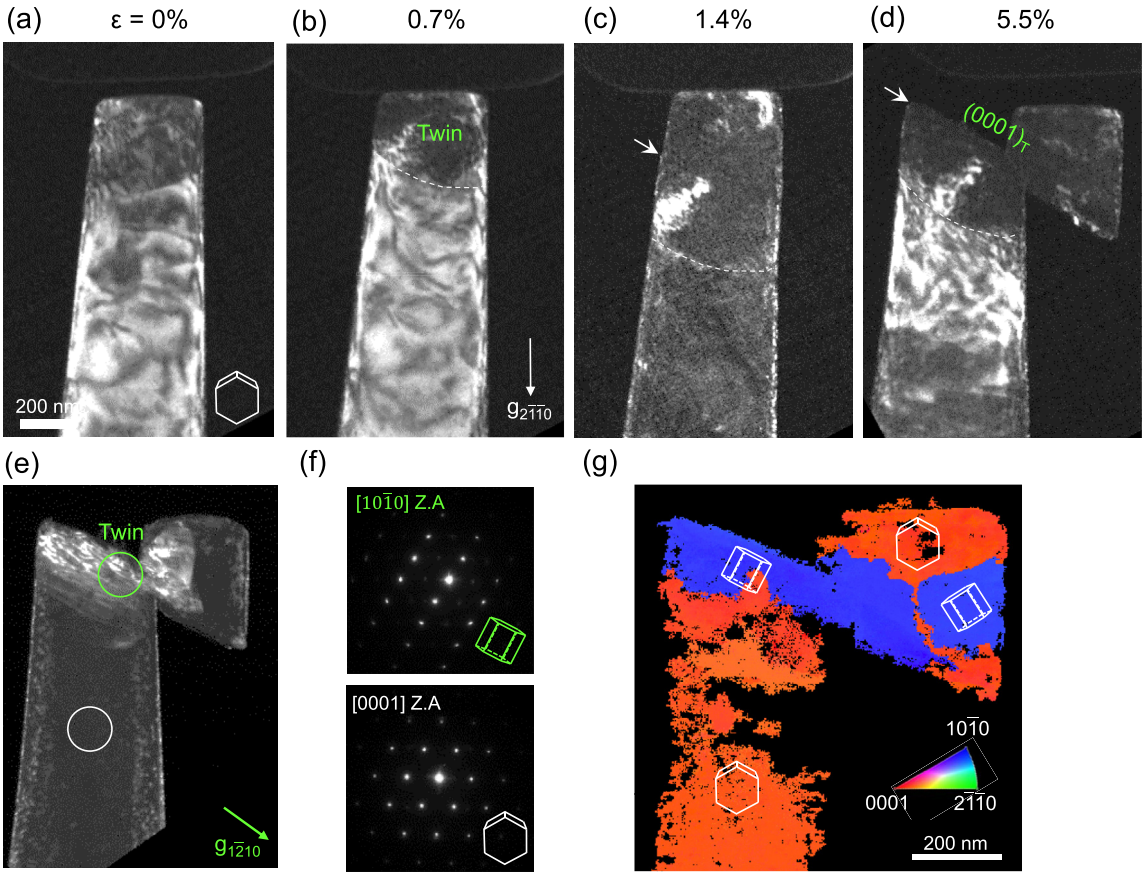

Fig. 11. In-situ TEM microcompression results of a 0.5 μm Mg [2$\bar{1}\bar{1}$0] pillar at a strain rate of 10^{-2} s^{-1}. (a) Before deformation ($\varepsilon = 0\%$); (b) Nucleation and propagation of the {10$\bar{1}$2} twin ($\varepsilon = 0.7\%$); (c) Thickening of the {10$\bar{1}$2} twin ($\varepsilon = 1.4\%$); (d) Localized basal slip within the twin ($\varepsilon = 5.5\%$); (e) TEM image showing the deformed pillar after compression to 5.5% strain. (f) Selected area diffraction patterns (SADPs) obtained from the twin ([10$\bar{1}$0] zone axis) and the matrix ([0001] zone axis). The corresponding in-situ TEM movie is provided as Supplementary Movie S11. (g) TEM orientation map of the deformed pillar showing the {10$\bar{1}$2} twin related orientation relationship between twin and matrix.

Considering that there are no internal obstacles blocking the dislocation motion in the single crystal pillars, the pile-up of prismatic <*a*> dislocations must be related to the intrinsic property of dislocations, that is, the lower mobility of the screw component due to the higher Peierls stress [10,45]. The prismatic <*a*> dislocations nucleating at the contact with the tip bow out along the inclined prismatic plane, but further expansion required for source operation is limited by the low mobility of the arms with screw character (Fig. 7). The sessile dislocation half-loops can react with each other to annihilate their arms, resulting a larger half-loop (refer to the schematic in Fig. 7e). As such, successively formed dislocation half-loops are piled up and the area in front of the half-loop is highly

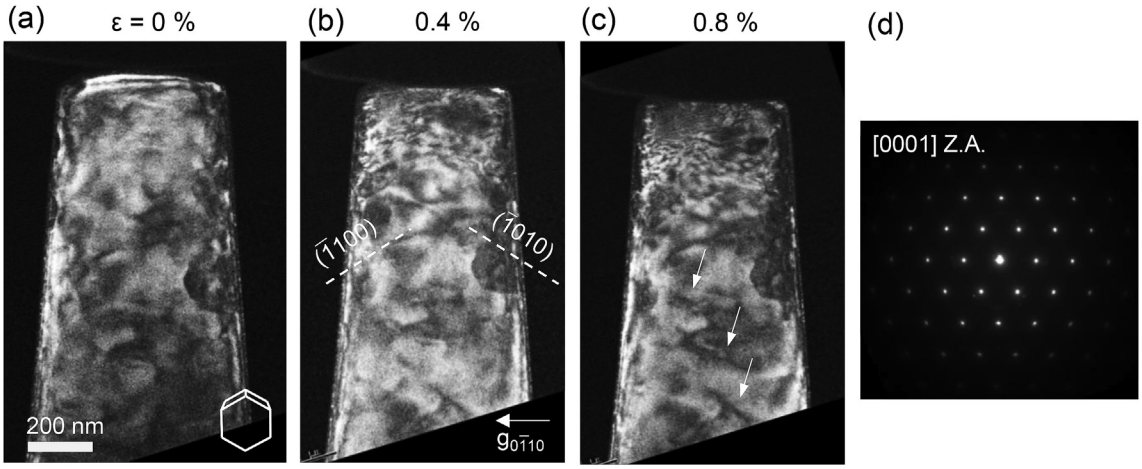

Fig. 12. In-situ TEM microcompression results of a 0.5 μm Mg $[2\bar{1}\bar{1}0]$ pillar at a strain rate of 10^{-4} s^{-1}. The viewing direction is close to [0001], which gives an almost edge-on view of the prismatic slip planes. (a) Before deformation ($\varepsilon = 0\%$); (b–c) Initial deformation by nucleation and glide of prismatic dislocations on the $(\bar{1}100)$ and $(\bar{1}010)$ prismatic planes (dashed lines). The dislocation line contrast (white arrows) suggests the dislocation slip along the basal slip ($\varepsilon = 0.8\%$); (d) SADP obtained from the deformed pillar. The [0001] zone axis diffraction pattern remained unchanged, indicating that no twin formed. The corresponding in-situ TEM movie is provided as Supplementary Movie S8.

stressed.

The twin nucleus does not form directly from the pile-up of prismatic <*a*> dislocations. Before the twin nucleation, the prismatic <*a*> dislocations cross-slip to the basal plane and dissociate into partial dislocations, one of which glides away and trails a SF behind (Fig. 8). The dissociation reaction appeared to occur from both arms of half-loops in the pile-up, separately and one after the other, resulting in the formation of two parallel basal SF ribbons. After the consecutive dislocation dissociation reactions, a twin nucleates at the junction between prismatic <*a*> dislocation and basal SFs. The present in-situ TEM reveals that not only the dislocation pile-up, but also the dissociation reactions of <*a*> dislocations resulting in the formation of SFs play critical roles in the nucleation of $\{10\bar{1}2\}$ twins.

Dislocation dissociation reactions are necessarily involved in most twinning dislocation-based models developed for $\{10\bar{1}2\}$ twinning in Mg [19,20,58]. This is due to the fact that the twin plane is not a slip plane, so that no ordinary glissile dislocations are allowed to glide on the $\{10\bar{1}2\}$ twin plane. Thus, dissociation reaction of a glissile dislocation leading to the formation of twinning dislocation is usually non-coplanar and as a consequence a residual dislocation (a kind of stair rod dislocation) remains at the junction between slip plane and twin plane. It is important to emphasize that the dislocation pile-up has two roles in the nonplanar dissociation. First, it can supply the stress needed for the dissociation of the leading <*a*> dislocation in pile-up. In most cases, the dissociation reactions are energetically unfavorable, so that stress concentrations from a dislocation pile-up are required to drive the dissociation reactions [20,58]. Second, after dissociation the dislocation pile-up helps the partial dislocations to overcome any attractive forces and trail a stable extension of a SF sufficiently far away from the reaction center. According to Capolungo and Beyerlein [20], the extension of SFs is important, as the larger the glide extension of the lead dislocation in a pile-up, the more likely the twinning dislocation can break away and trigger further events that lead to either formation of the twin nucleus or successive twin growth.

The twin nucleation occurs very fast and completed within one movie frame (0.04 s) in most cases, resulting in the sudden appearance of a finite size of twinned region (Fig. 9a and b). The size of the smallest twinned region measured by TEM is ~50 nm in width and ~140 nm in length. The fact that we always observe the sudden appearance of a twin with a finite size implies the existence of a stable nucleus size, where stable means that under the applied stress, the twin nucleus either retains its configuration or propagates as a twin into the crystal without shrinkage [21]. Whether twinning proceeds after the dissociation reactions depends on whether a stable twin nucleus can form or not. It is worth noting that a back stress is imposed on the twin embryo by the surrounding matrix due to the volume change by lattice reorientation. The formation of a stable twin nucleus is likely to be suppressed by this back stress. If the applied stress is not relaxed by dislocation slip but increased to overcome the back stress during compression, the stress will be relaxed by twin nucleation. The critical volume (or thickness) of a twin for relaxation of the accumulated stress is different as the local stress state is likely to be different for each pillar as observed in Fig. 9. These results imply another distinction between twins in HCP metals and cubic metals in terms of the size of twin nucleus – unlike the stable twin nuclei in cubic metals, the $\{10\bar{1}2\}$ twin nucleus is not constructed by adjacent layers of twinning dislocations [18]; For both BCC and FCC metals, the likely structure of the twin nucleus apparently consists of three adjacent planes of low energy SFs [21]. It is reasonable to assume that the smallest twin size we detected by in-situ TEM must be much larger than the stable nucleus size, since it most likely already underwent transverse propagation and even thickening after nucleation within the time range of one video frame.

It is conceivable to assume that there must be a precursor for the formation of TB, from which a reoriented crystal (twin embryo) forms and grows to reach the stable size. Recent atomistic simulation by Zu et al. [59] reported that a partial pyramidal dislocation glides on the pyramidal $\{10\bar{1}1\}$ plane with a Burgers vector of $1/4 < 10\bar{1}2 >$ and features a SF behind its leading front. Subsequently, a reoriented crystal (twin) nucleates from the surface site where the partial pyramidal dislocation previously initiates. It appears that the SF trailed by partial dislocation acts as a precursor for the formation of TB, along which atomic shuffling forms twin embryos. These embryos expand and coalesce into a single, larger nucleus with time. According to DFT calculations, the associated transformation stresses are large (~3 GPa), supporting the notion that the SFs, where high stresses and heterogeneities are located, are preferred sites for the twin nucleation [22].

Although the present in-situ TEM experiments captured the moment of twin nucleation, the results are limited in assessing the

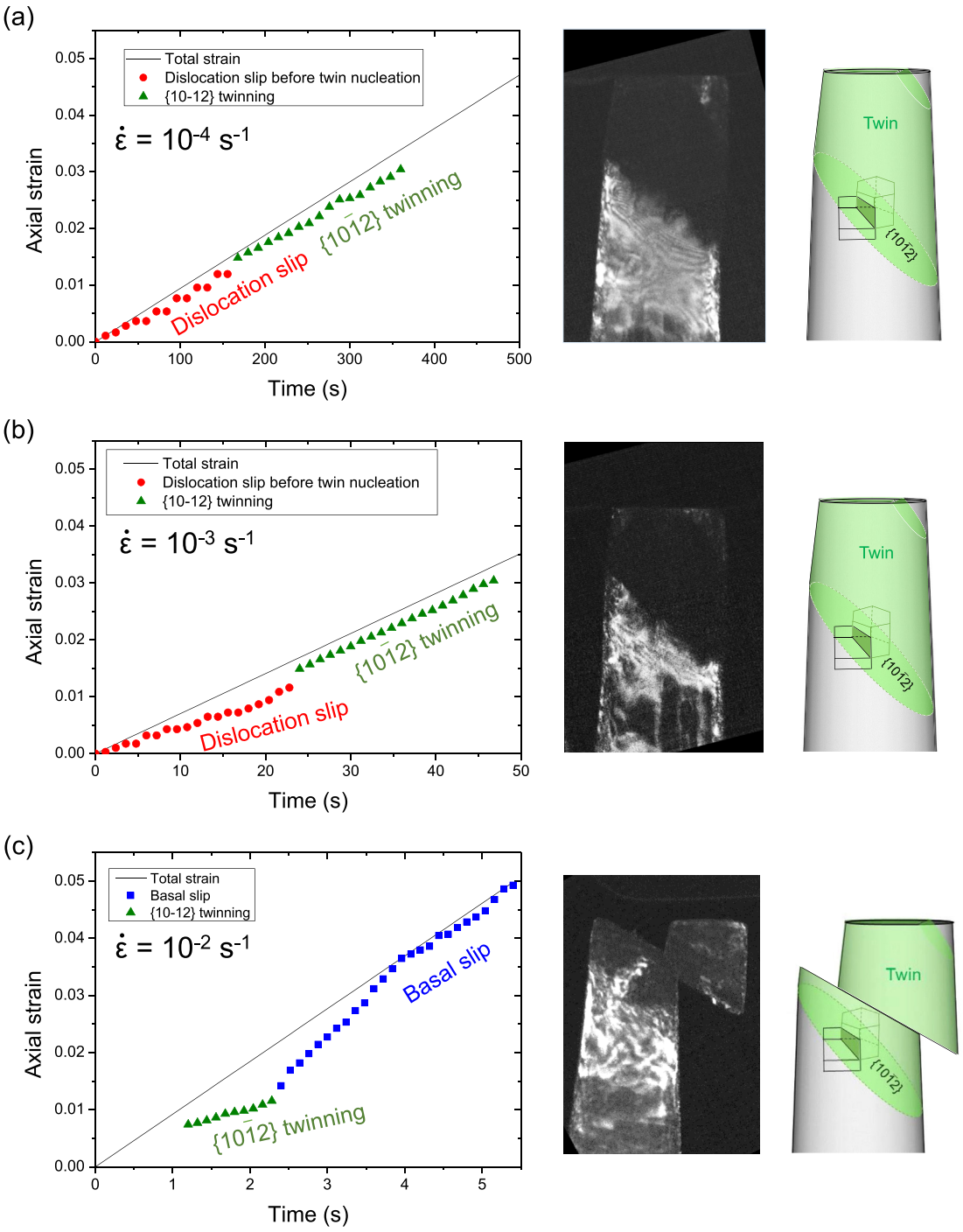

Fig. 13. Tracing of the axial strain of 0.5 μm Mg [2$\bar{1}\bar{1}$0] pillars with deformation time during microcompression in the TEM at various strain rates. Plot of axial strain vs. time at the strain rate of: (a) 10^{-4} s^{-1}; (b) 10^{-3} s^{-1}; (c) 10^{-2} s^{-1}. The applied strain is shown as straight line. The axial strain measured using frame images of TEM movies is indicated by symbol in each plot. Different symbols and colors are used to distinguish different deformation mode, e.g., red circles for dislocation slip, green triangles for {10$\bar{1}$2} twinning and blue squares for the basal slip within the twin. For each strain rate a TEM image and schematic are shown to represent the dominant deformation mode. The corresponding in-situ TEM movie and strain analysis are provided as Supplementary Movie S9, S10 and S11 for the strain rate of 10^{-4} s^{-1}, 10^{-3} s^{-1}, and 10^{-2} s^{-1}, respectively. (For interpretation of the references to color in this figure legend, the reader is referred to the Web version of this article.)

nucleation mechanism, i.e. as to how the twin nucleus forms and reaches the stable size. However, we note that the twinned region appeared first from the dislocation junction and its moving tips are often bounded by the basal SFs extended from the dislocation junction (Fig. 9a and b). This twin morphology indicates that the basal SF may act as a precursor to the twin nucleation by promoting basal-prismatic (BP) transformation. Once a stable twin nucleus is formed, the transverse propagation occurs too fast to be detected. After transverse propagation, the TB becomes parallel to the{10$\bar{1}$2} twin plane with only small local deviations (Fig. 9a and b).

It appears that the thickening of the twin by TB migration does not occur in a layer-by-layer advancement via sequential glide of twinning dislocations [60], as the TB is gradually deviating from the $\{10\bar{1}2\}$ twin plane during thickening (Fig. 10). Although there exist many dislocations ahead of the moving TB, it is not clear whether they are twinning dislocations gliding on the TB, misfit dislocations accommodating the lattice mismatch between twin and matrix, or emissary dislocations [61]. It is also shown that the moving TBs constantly develop roughness, as the TB does not migrate as a whole but partially. Not only the array of dislocations in front of the TB, but also the rugged morphology with the existence of BP and PB interfaces make it difficult to resolve the active twin growth mechanism from shear-dominant and suffle dominant models. Further elaborate in-situ TEM observation of twinning process at higher spatial and temporal resolution is required.

4.2. Size effects in twin nucleation and growth

The deformation twinning of HCP metals has been shown to exhibit a pronounced crystal size effect, i.e. the smaller the crystal, the greater the stress for twin nucleation. As a quantitative measure of the size effect, the power-law exponent (n) measured in this study is 0.70 ± 0.20 (Fig. 3), which is close to the value of 0.77 reported for the $\{10\bar{1}2\}$ twinning by Sim et al. [10], but smaller than that obtained from the tensile straining tests along $[10\bar{1}0]$ loading axis ($n = 0.93$) by Kim [53]. Interestingly, many deformation twinning modes of HCP metals show stronger size effects than competing dislocation slip. For example, the size exponent for the basal slip in Mg was reported as 0.64–0.77 [53,62]. As such, with decreasing crystal size the stress for twin nucleation increases more steeply than that for dislocation nucleation. It has been shown that a critical size exists in HCP metals, usually ~1 μm or smaller, below which deformation twinning is hardly activated but dislocation slip becomes dominant [8,10].

It is worth noting that the size-dependent competition/transition between twinning and slip in HCP metals is opposite to what is usually exhibited by FCC metals, that is, deformation twinning is preferred below the critical size [33,34]. In FCC metals, the mechanism of dislocation slip and deformation twinning are in principle the same as both occur by local shear by dislocation glide. The preference of twinning in small size FCC metals is due to the fact that less energy (stress) is required to extend SF by glide of a leading partial (twinning) dislocation, since the width of SF scales with the crystal size. To understand the size effects of deformation twinning in HCP metals one has to understand the twinning mechanism and its interplay with the crystal size.

Several explanations have been made to account for the size effects on deformation twinning of HCP metals. Yu et al. [8] proposed a 'stimulated slip' model, in which correlated layer-by-layer shearing occurs via glide of each twinning dislocation on atomically adjacent planes, which is similar to the pole mechanism. According to the model, the size effect arises from the fact that the number of dislocations which can act as promoter of twinning decreases with sample size. However, this model would be valid only for an ideal shear-dominant twinning mode, i.e. one that occurs by glide of twinning dislocations on a twin plane, but this is not the case for the $\{10\bar{1}2\}$ twinning in Mg as Wang et al. [22] have shown by density functional theory. A recent study by Sim et al. [10] noticed the important role of sessile screw dislocations on prismatic planes for the nucleation of $\{10\bar{1}2\}$ twins and pointed out that they act as local stress concentrators for twin nucleation. The relative magnitude of the resolved shear stress with respect to the CRSS of screw dislocation determines whether it glides (and acts as a dislocation source) or remains sessile (and activates the nucleation of a twin). Since smaller crystals yield under higher stresses, the screw dislocation easily gives way to glide under such high shear stresses, so that the deformation is governed by dislocation slip.

The present in-situ observations revealed that the nucleation of $\{10\bar{1}2\}$ twins is facilitated by dislocation processes. Thus, the size effect on the $\{10\bar{1}2\}$ twin nucleation is closely related as to how the dislocation processes are affected by the crystal size. First of all, the average source size of prismatic <*a*> dislocations decreases with decreasing crystal size, requiring a larger stress in smaller pillars [63]. However, such size effect based on source size alone would result in a similar size effect as for dislocation slip. Apart from the size effect originating from dislocation sources, the most critical step in the $\{10\bar{1}2\}$ twin nucleation would be the local stress concentration at the dislocation pile-up and subsequently formed dislocation junctions by dissociation reactions right before the twin nucleation. Therefore, compared with the ordinary crystal size effect associated with the activation of dislocation sources, a much larger stress is needed to drive the dissociation reaction of dislocations due to the back stress from the dislocation pile-up [64]. As the length scale of dislocation pile-up and following dislocation junction formation would also scale with the crystal size, a larger stress is required for twin nucleation compared to that needed for dislocation source operation [65]. Therefore, the stronger size effect of the $\{10\bar{1}2\}$ twinning may arise from the precursor to twin nucleation, that is dislocation pile-up and junction formation, which depends more strongly on the crystal size than the ordinary dislocation source operation.

Since the twin nucleation stress is higher than the twin propagation stress, when a twin nucleates it subsequently propagates down the pillar before another twin nucleates. As twin propagation is governed by long range stresses whereas twin nucleation is governed by the local stress state near the dislocation pile-up, the size effect of twin propagation ($n = 0.47$) is not as pronounced as that of twin nucleation ($n = 0.70$).

4.3. Effect of strain rate on the twin-mediated deformation

Deformation twinning is preferred in HCP metals at higher strain rates because this can effectively raise the stress to the level required for twin nucleation [66]. In the case of $\{10\bar{1}2\}$ twinning in Mg, a similar rate dependent behavior was reported, i.e. increasing strain rate promotes $\{10\bar{1}2\}$ twinning [35,36]. In addition to twin nucleation, higher strain rates activate basal slip within the twinned region at lower strain during twin propagation.

For the nucleation of a $\{10\bar{1}2\}$ twin, as discussed in previous sections, local stress concentration is required. At low strain rate, the dislocation pile-up and dislocation junction act as local stress concentrator for twin nucleation. At higher strain rate, before the formation of a dislocation pile-up, individual dislocations can act as local stress concentrator because glide of dislocations is kinetically suppressed, which increases the perturbation of the local stress states. This depends on the character of the dislocation and the Peierls stress for each slip system, e.g. screw dislocations on the prismatic plane have the highest Peierls stress and therefore are the most probable local stress concentrator at high strain rates [45]. As a result, the nucleation and transverse propagation of a $\{10\bar{1}2\}$ twin can be prevalent at high strain rate deformation.

The reason why increasing the strain rate subsequently promotes the activation of basal slip within the twinned region is likely related to the kinetics of the TB migration during the twin thickening process. While transverse propagation of a $\{10\bar{1}2\}$ twin occurs quickly after twin nucleation, the twin thickening process is relatively slow, driven by long range stress fields. We observed that the TB is gradually deviating from the $\{10\bar{1}2\}$ twin plane and becomes rugged during twin thickening (Fig. 10). This implies that BP

transformation is likely to occur along the moving TB. When the TB morphology consists of the BP interfaces and coherent TBs, the twinning disconnection at the TB decomposes into climb and glide components [67,68]. The movement of TBs can be kinetically suppressed due to the alternating movement of climb and glide components during twin thickening at high strain rates and, thus, the activation of basal slip within the twinned region is preferred.

5. Conclusion

We have carried out in-situ microcompression of Mg $[2\bar{1}\bar{1}0]$ pillars in SEM and TEM to investigate the size and strain rate effects on the deformation behavior. It was observed that the nucleation and growth of a single $\{10\bar{1}2\}$ twin variant dominates the deformation of pillars. The nucleation mechanism of $\{10\bar{1}2\}$ twin assessed by in-situ TEM directly showed that the pile-up of prismatic <*a*> dislocations acts as a local stress concentration for the twin nucleation. The twin nucleus does not form directly from the pile-up of prismatic <*a*> dislocations. Instead, the prismatic <*a*> dislocations cross-slip to the basal plane and dissociate into partial dislocations, one of which glides away and trails a SF behind. After consecutive dislocation dissociation reactions, a twin nucleus appeared at the junction between <*a*> dislocations and basal SFs. The present in-situ TEM reveals that not only the dislocation pile-up but also the dissociation reaction of <*a*> dislocations resulting in the formation of SFs play critical roles in the nucleation of $\{10\bar{1}2\}$ twins in single crystal Mg pillars under compression. The twin nucleation was very fast, resulting in the sudden appearance of a finite sized twinned region, implying the existence of a stable nucleus size.

The $\{10\bar{1}2\}$ twinning exhibits a relatively strong size effect in the twin nucleation stress ($n = 0.7$). As the length scale of dislocation pile-up and also the following dislocation junction formation scale with the crystal size, a larger stress is required with a decrease of the crystal size compared to that needed for the ordinary dislocation source operation.

For the high strain rate deformation, as the rate of the axial strain produced by the growth of $\{10\bar{1}2\}$ twin is too low to accommodate the applied strain at a given time, strain energy accumulates and increases with the applied strain. When the twin grows to reach the required twin thickness for basal slip, this mode promptly activates to release the accumulated strain energy and swiftly catches up to the applied strain. However, at the strain rate of 10^{-4} s^{-1}, extensive prior dislocation activities, mostly prismatic slip with sporadic activation of basal slip along the axial direction, were observed up to 1% strain before the twin nucleation commenced. It is evident that prismatic slip and $\{10\bar{1}2\}$ twinning can effectively accommodate the imposed strain at any given time for the low strain rate deformation, so that the accumulation of strain energy is not so significant. Although favored by the Schmid factor, the activation of basal slip within the twinned region competes with the twin propagation and is determined by the strain energy accumulated within the twin as a consequence of rate-limiting strain release by twin propagation.

Acknowledgements

This work was supported by the Creative Materials Discovery Program through the National Research Foundation (NRF) of Korea funded by the Ministry of Science, ICT and Future Planning (NRF-2015M3D1A1070672), Bio-inspired Innovation Technology Development Project (NRF-2018M3C1B7021994), NRF grant (NRF-2015R1A2A2A01007904) and Industrial Technology Innovation Program (10080654) of the Ministry of Trade, Industry & Energy (MOTIE, Korea). Further financial support by the Austrian Science Fund FWF (project number I-1020) is gratefully acknowledged.

Appendix A. Supplementary data

Supplementary data related to this article can be found at https://doi.org/10.1016/j.actamat.2018.07.027.

References

[1] J.W. Christian, S. Mahajan, Deformation twinning, Prog. Mater. Sci. 39 (1995) 1–157.
[2] M.H. Yoo, Slip, twinning, and fracture in hexagonal close-packed metals, Metall. Trans. A 12 (1981) 409–418.
[3] C. Bettles, M. Barnett, Advances in Wrought Magnesium Alloys: Fundamentals of Processing, Properties and Applications, first ed., Woodhead, Cambridge, 2012.
[4] S.R. Agnew, Ö. Duygulu, Plastic anisotropy and the role of non-basal slip in magnesium alloy AZ31B, Int. J. Plast. 21 (2005) 1161–1193.
[5] J. Koike, Enhanced deformation mechanisms by anisotropic plasticity in polycrystalline Mg alloys at room temperature, Metall. Mater. Trans. A 36 (2005) 1689–1696.
[6] D.W. Brown, S.R. Agnew, M.A.M. Bourke, T.M. Holden, S.C. Vogel, C.N. Tomé, Internal strain and texture evolution during deformation twinning in magnesium, Mater. Sci. Eng. A 399 (2005) 1–12.
[7] J.R. Greer, J.T.M. De Hosson, Plasticity in small-sized metallic systems: intrinsic versus extrinsic size effect, Prog. Mater. Sci. 56 (2011) 654–724.
[8] Q. Yu, Z.-W. Shan, J. Li, X. Huang, L. Xiao, J. Sun, E. Ma, Strong crystal size effect on deformation twinning, Nature 463 (2010) 335–338.
[9] Q. Yu, L. Qi, R.K. Mishra, J. Li, A.M. Minor, Reducing deformation anisotropy to achieve ultrahigh strength and ductility in Mg at the nanoscale, Proc. Natl. Acad. Sci. 110 (2013) 13289–13293.
[10] G.D. Sim, G. Kim, S. Lavenstein, M.H. Hamza, H. Fan, J.A. El-Awady, Anomalous hardening in magnesium driven by a size-dependent transition in deformation modes, Acta Mater. 144 (2018) 11–20.
[11] H. Fan, S. Aubry, A. Arsenlis, J.A. El-Awady, Grain size effects on dislocation and twinning mediated plasticity in magnesium, Scripta Mater. 112 (2016) 50–53.
[12] H. El Kadiri, C.D. Barrett, J. Wang, C.N. Tomé, Why are $\{10\bar{1}2\}$ twins profuse in magnesium? Acta Mater. 85 (2015) 354–361.
[13] M.M. Avedesian, H. Baker, A.S.M.I.H. Committee, ASM Specialty Handbook: Magnesium and Magnesium Alloys, ASM International, Materials Park, OH, 1999.
[14] B. Li, E. Ma, Atomic shuffling dominated mechanism for deformation twinning in magnesium, Phys. Rev. Lett. 103 (2009), 035503.
[15] B. Li, X.Y. Zhang, Twinning with zero twinning shear, Scripta Mater. 125 (2016) 73–79.
[16] R.C. Pond, J.P. Hirth, Defects at surfaces and interfaces, Solid State Phys. 47 (1994) 287–365.
[17] J. Wang, J.P. Hirth, C.N. Tomé, $(\bar{1}012)$ Twinning nucleation mechanisms in hexagonal-close-packed crystals, Acta Mater. 57 (2009) 5521–5530.
[18] J. Wang, R.G. Hoagland, J.P. Hirth, L. Capolungo, I.J. Beyerlein, C.N. Tomé, Nucleation of a $(\bar{1}012)$ twin in hexagonal close-packed crystals, Scripta Mater. 61 (2009) 903–906.
[19] S. Mendelson, Dislocation dissociations in hcp metals, J. Appl. Phys. 41 (1970) 1893–1910.
[20] L. Capolungo, I.J. Beyerlein, Nucleation and stability of twins in hcp metals, Phys. Rev. B 78 (2008), 024117.
[21] I.J. Beyerlein, X. Zhang, A. Misra, Growth twins and deformation twins in metals, Annu. Rev. Mater. Res. 44 (2014) 329–363.
[22] J. Wang, S.K. Yadav, J.P. Hirth, C.N. Tomé, I.J. Beyerlein, Pure-shuffle nucleation of deformation twins in hexagonal-close-packed metals, Mater. Res. Lett. 1 (2013) 126–132.
[23] B. Xu, L. Capolungo, D. Rodney, On the importance of prismatic/basal interfaces in the growth of $(\bar{1}012)$ twins in hexagonal close packed crystals, Scripta Mater. 68 (2013) 901–904.
[24] X.Y. Zhang, B. Li, X.L. Wu, Y.T. Zhu, Q. Ma, Q. Liu, P.T. Wang, M.F. Horstemeyer, Twin boundaries showing very large deviations from the twinning plane, Scripta Mater. 67 (2012) 862–865.
[25] B. Li, X.Y. Zhang, Global strain generated by shuffling-dominated twinning, Scripta Mater. 71 (2014) 45–48.
[26] B.-Y. Liu, L. Wan, J. Wang, E. Ma, Z.-W. Shan, Terrace-like morphology of the boundary created through basal-prismatic transformation in magnesium, Scripta Mater. 100 (2015) 86–89.
[27] B.-Y. Liu, J. Wang, B. Li, L. Lu, X.-Y. Zhang, Z.-W. Shan, J. Li, C.-L. Jia, J. Sun, E. Ma, Twinning-like lattice reorientation without a crystallographic twinning plane, Nat. Commun. 5 (2014) 3297.
[28] E. Lilleodden, Microcompression study of Mg (0 0 0 1) single crystal, Scripta Mater. 62 (2010) 532–535.
[29] C.M. Byer, B. Li, B. Cao, K.T. Ramesh, Microcompression of single-crystal magnesium, Scripta Mater. 62 (2010) 536–539.
[30] C.M. Byer, K.T. Ramesh, Effects of the initial dislocation density on size effects in single-crystal magnesium, Acta Mater. 61 (2013) 3808–3818.

[31] Q. Yu, L. Qi, K. Chen, R.K. Mishra, J. Li, A.M. Minor, The nanostructured origin of deformation twinning, Nano Lett. 12 (2012) 887–892.
[32] K.E. Prasad, K. Rajesh, U. Ramamurty, Micropillar and macropillar compression responses of magnesium single crystals oriented for single slip or extension twinning, Acta Mater. 65 (2014) 316–325.
[33] M. Chen, E. Ma, K.J. Hemker, H. Sheng, Y. Wang, X. Cheng, Deformation twinning in nanocrystalline aluminum, Science 300 (2003) 1275–1277.
[34] Y.T. Zhu, X.Z. Liao, X.L. Wu, Deformation twinning in nanocrystalline materials, Prog. Mater. Sci. 57 (2012) 1–62.
[35] I. Ulacia, N.V. Dudamell, F. Gálvez, S. Yi, M.T. Pérez-Prado, I. Hurtado, Mechanical behavior and microstructural evolution of a Mg AZ31 sheet at dynamic strain rates, Acta Mater. 58 (2010) 2988–2998.
[36] N.V. Dudamell, I. Ulacia, F. Gálvez, S. Yi, J. Bohlen, D. Letzig, I. Hurtado, M.T. Pérez-Prado, Twinning and grain subdivision during dynamic deformation of a Mg AZ31 sheet alloy at room temperature, Acta Mater. 59 (2011) 6949–6962.
[37] T. Zhu, J. Li, A. Samanta, A. Leach, K. Gall, Temperature and strain-rate dependence of surface dislocation nucleation, Phys. Rev. Lett. 100 (2008), 025502.
[38] R.J. Asaro, S. Suresh, Mechanistic models for the activation volume and rate sensitivity in metals with nanocrystalline grains and nano-scale twins, Acta Mater. 53 (2005) 3369–3382.
[39] X.L. Nan, H.Y. Wang, L. Zhang, J.B. Li, Q.C. Jiang, Calculation of Schmid factors in magnesium: analysis of deformation behaviors, Scripta Mater. 67 (2012) 443–446.
[40] G. Moser, H. Felber, B. Rashkova, P.J. Imrich, C. Kirchlechner, W. Grosinger, C. Motz, G. Dehm, D. Kiener, Sample preparation by metallography and focused ion beam for nanomechanical testing, Pract. Metallogr. 49 (2012) 343–355.
[41] D. Kiener, C. Motz, M. Rester, M. Jenko, G. Dehm, FIB damage of Cu and possible consequences for miniaturized mechanical tests, Mater. Sci. Eng. A 459 (2007) 262–272.
[42] J. Jeong, S. Lee, Y. Kim, S.M. Han, D. Kiener, Y.-B. Kang, S.H. Oh, Microstructural evolution of a focused ion beam fabricated Mg nanopillar at high temperatures: defect annihilation and sublimation, Scripta Mater. 86 (2014) 44–47.
[43] P. Oleynikov, S. Hovmöller, X.D. Zou, Precession electron diffraction: observed and calculated intensities, Ultramicroscopy 107 (2007) 523–533.
[44] E. Schmid, Beiträge zur Physik und Metallographie des Magnesiums, Zeitschrift Für Elektrochemie Und Angew. Phys. Chemie 37 (1931) 447–459.
[45] J.A. Yasi, T. Nogaret, D.R. Trinkle, Y. Qi, L.G. Hector, W.A. Curtin, Basal and prism dislocation cores in magnesium: comparison of first-principles and embedded-atom-potential methods predictions, Model. Simulat. Mater. Sci. Eng. 17 (2009), 055012.
[46] P.W. Bakarian, C.H. Mathewson, Slip and twinning in magnesium single crystals at elevated temperatures, Trans. AIME 152 (1943) 226–253.
[47] H. Conrad, W.D. Robertson, Effect of temperature on the flow stress and strain-hardening coefficient of magnesium single crystals, JOM 9 (1957) 503–512.
[48] R.E. Reed-Hill, W.D. Robertson, Deformation of magnesium single crystals by nonbasal slip, JOM 9 (1957) 496–502.
[49] P. Ward Flynn, J. Mote, J.E. Dorn, On the thermally activated mechanism of prismatic slip in magnesium single crystals, Trans. Metall. Soc. AIME 221 (1961) 1148–1154.
[50] S. Ando, K. Nakamura, K. Takashima, H. Tonda, $\{11\bar{2}2\}<\bar{1}123>$ slip in magnesium single crystal, J. Japan Inst. Light Met 42 (1992) 765–771.
[51] H. Fan, J.A. El-Awady, Towards resolving the anonymity of pyramidal slip in magnesium, Mater. Sci. Eng. A 644 (2015) 318–324.
[52] E.W. Kelly, W.F. Hosford, Plane-strain compression of magnesium and magnesium alloy crystals, Trans. Metall. Soc. AIME 242 (1968) 5–13.
[53] G.S. Kim, Small Volume Investigation of Slip and Twinning in Magnesium Single Crystals, PhD thesis, Universite de Grenoble, Grenoble, 2011.
[54] A. Couret, D. Caillard, W. Püschl, G. Schoeck, Prismatic glide in divalent h.c.p. metals, Philos. Mag. 63 (1991) 1045–1057.
[55] J. Wang, I.J. Beyerlein, C.N. Tomé, An atomic and probabilistic perspective on twin nucleation in Mg, Scripta Mater. 63 (2010) 741–746.
[56] I.J. Beyerlein, C.N. Tome, A probabilistic twin nucleation model for HCP polycrystalline metals, Proc. R. Soc. A 466 (2010) 2517–2544.
[57] I.J. Beyerlein, L. Capolungo, P.E. Marshall, R.J. McCabe, C.N. Tome, Statistical analyses of deformation twinning in magnesium, Philos. Mag. 90 (2010) 2161–2190.
[58] H. Feng, Q.H. Fang, B. Liu, Y. Liu, Y.W. Liu, P.H. Wen, Nucleation and growth mechanisms of nanoscale deformation twins in hexagonal-close-packed metal magnesium, Mech. Mater. 109 (2017) 26–33.
[59] Q. Zu, X.Z. Tang, S. Xu, Y.F. Guo, Atomistic study of nucleation and migration of the basal/prismatic interfaces in Mg single crystals, Acta Mater. 130 (2017) 310–318.
[60] J. Wang, I.J. Beyerlein, J.P. Hirth, Nucleation of elementary $\{\bar{1}011\}$ and $\{\bar{1}013\}$ twinning dislocations at a twin boundary in hexagonal close-packed crystals, Model. Simul. Mater. Sci. Eng. 20 (2012), 024001.
[61] S. Vaidya, S. Mahajan, Accommodation and formation of $\{11\bar{2}1\}$ twins in Co single crystals, Acta Metall. 28 (1980) 1123–1131.
[62] J. Ye, R.K. Mishra, A.K. Sachdev, A.M. Minor, In situ TEM compression testing of Mg and Mg-0.2 wt.% Ce single crystals, Scripta Mater. 64 (2011) 292–295.
[63] T.A. Parthasarathy, S.I. Rao, D.M. Dimiduk, M.D. Uchic, D.R. Trinkle, Contribution to size effect of yield strength from the stochastics of dislocation source lengths in finite samples, Scripta Mater. 56 (2007) 313–316.
[64] B. Pan, Y. Shibutani, X. Zhang, F. Shang, Effect of dislocation pile-up on size-dependent yield strength in finite single-crystal micro-samples, J. Appl. Phys. 118 (2015), 014305.
[65] D. Mordehai, S.W. Lee, B. Backes, D.J. Srolovitz, W.D. Nix, E. Rabkin, Size effect in compression of single-crystal gold microparticles, Acta Mater. 59 (2011) 5202–5215.
[66] M.A. Meyers, O. Vöhringer, V.A. Lubarda, The onset of twinning in metals: a constitutive description, Acta Mater. 49 (2001) 4025–4039.
[67] J. Wang, L. Liu, C.N. Tomé, S.X. Mao, S.K. Gong, Twinning and de-twinning via glide and climb of twinning dislocations along serrated coherent twin boundaries in hexagonal-close-packed metals, Mater. Res. Lett. 1 (2013) 81–88.
[68] A. Serra, D.J. Bacon, A new model for $\{10\bar{1}2\}$ twin growth in hcp metals, Philos. Mag. A 73 (1996) 333–343.